

Fluorescence Triggered by Radioactive β Decay in Optimized Hyperbolic Cavities

J. Abad-Arredondo¹, F.J. García-Vidal,^{1,2} Q. Zhang,^{3,4} E. Khwaja^{1,3,4}, V.M. Menon,^{5,6}
J. Grimm^{1,4,7,8,9} and A.I. Fernández-Domínguez^{1,*}

¹Departamento de Física Teórica de la Materia Condensada and Condensed Matter Physics Center, Universidad Autónoma de Madrid, 28049 Madrid, Spain

²Donostia International Physics Center, 20018 San Sebastián, Spain

³Department of Chemistry, Hunter College, Graduate Center of the City University of New York, New York, New York 10016, USA

⁴Department of Radiology, Memorial Sloan Kettering Cancer Center, New York, New York 10065, USA

⁵Department of Physics, Graduate Center of the City University of New York, New York, New York 10016, USA

⁶Department of Physics, City College of the City University of New York, New York, New York 10031, USA

⁷Molecular Pharmacology Program, Memorial Sloan Kettering Cancer Center, New York, New York 10065, USA

⁸Pharmacology Program, Weill Cornell Medical College, New York, New York, USA

⁹Department of Radiology, Weill Cornell Medical College, New York, New York, USA



(Received 3 June 2020; revised 20 July 2020; accepted 23 July 2020; published 27 August 2020)

Luminescence arising from β decay of radiotracers has attracted much interest recently as a viable *in vivo* imaging technique. The emitted Cerenkov radiation can be directly detected by high-sensitivity cameras or used to excite highly efficient fluorescent dyes. Here we investigate the enhancement of visible and infrared emission driven by β decay of radioisotopes in the presence of a hyperbolic nanocavity. By means of a transfer-matrix approach, we obtain quasianalytic expressions for the fluorescence-enhancement factor at the dielectric core of the metalodielectric cavity, and report a 100-fold amplification in periodic structures. A particle-swarm optimization of the layered shell geometry reveals that enhancement of up to 10 000-fold is possible because of the hybridization and spectral overlap of whispering-gallery and localized-plasmon modes. Our findings may find application in nuclear-optical medical imaging, as they provide a strategy for the use of highly energetic gamma rays, Cerenkov luminescence, and visible and near-infrared fluorescence through the same nanotracer.

DOI: 10.1103/PhysRevApplied.14.024084

I. INTRODUCTION

Cerenkov luminescence [1] (CL), the electromagnetic (EM) radiation by superluminal charged particles in a given medium, has attracted much research attention lately in the context of medical imaging [2]. It was not until 2009 that this phenomenon was identified as naturally occurring in the decay of radionuclides (such as ^{18}F or ^{124}I) used in positron-emission tomography [3,4], a clinical technique instrumental for, among other applications, cancer diagnosis. This discovery opened the way to the use of radiotracers for bimodal imaging [5]: combining the Cerenkov photons emitted by β particles traveling through tissue and the gamma rays (on the order of approximately 100 keV) generated as a result of positron-electron annihilation in the vicinity of the radioisotope. This nuclear-optical approach can outperform conventional positron-emission tomography scanning in various aspects as it requires

shorter acquisition times and allows higher spatial resolution [6]. Importantly, in contrast to nuclear imaging, CL can also be tuned and modulated because of recent advances in nanotechnology [7].

The classical EM description of CL is based on the Frank-Tamm equation [8], which yields a power spectrum of the form $P(\omega) \propto \omega$ for a homogeneous, nondispersive host medium (such as human tissue). Thus, $P(\omega)$ is maximum in the UV region and decays monotonically in the visible range with decreasing frequency. Moreover, β particles in tissue meet the superluminal velocity threshold only within up to a few millimeters from the decaying radioisotopes. These spectral and spatial factors make CL extremely faint, orders of magnitude lower than ambient light [9]. This intrinsic low radiance is the main obstacle hindering the widespread implementation of CL-based medical imaging techniques.

Recently, nanophotonics science and technology have enabled unprecedented control over the spectral [10] and spatial [11] characteristics of Cerenkov radiation.

*a.fernandez-dominguez@uam.es

Theoretical and experimental reports have investigated metamaterial [12–14] and plasmonic [15–17] structures. However, the extended character of these devices prevents their application for clinical purposes. One of the most promising avenues for overcoming the limitations of CL for medical imaging consists in the combination of radiotracers and fluorescent agents with a large Stokes shift. In this scheme, known as secondary-Cerenkov-induced-fluorescence imaging (SCIFI) [18,19], quantum dots or dye molecules are attached to radiotracers. The former are excited by the near field of the CL generated in the radioactive decay of the latter, but their emission occurs in the visible and near-infrared regions, within the so-called biological transparency window [9]. Remarkably, this approach also allows minimization of the impact of two of the main constraints of conventional fluorescence imaging, the limited penetration depth and the tissue autofluorescence inherent to the external illumination [6,7].

In this article, we apply metamaterial and plasmonic ideas to SCIFI by designing spherical hyperbolic nanocavities [20] for enhanced fluorescence triggered by traveling β particles. These nanostructures consist of a dielectric core embedding a fluorescent emitter and surrounded by alternating nanometer-thick metal and dielectric layers, the spherical analog of indefinite bulk metamaterials [10,21]. We consider molecules with an intrinsic quantum yield of 100% (whose radiative efficiency cannot be increased) and negligible Stokes shift (unsuitable for conventional SCIFI). By means of a transfer-matrix approach based on a vector-spherical-harmonic expansion of the EM fields [22,23], we investigate the fluorescence spectrum of these nanostructures. We consider first perfectly periodic geometries, finding that an amplification of approximately 100 times can be attained in these cavities (compared with dielectric cavities of the same size) in two different spectral ranges. Next we use the quasianalytic character of our approach to perform a particle-swarm optimization (PSO) [24] of the metallocdielectric shell. This procedure gives rise to geometries with highly asymmetric layer distributions, in which whispering-gallery and localized-plasmon resonances hybridize and overlap spectrally to yield fluorescence-enhancement factors approaching 10^4 at operating frequencies in the near-infrared region.

II. THEORETICAL APPROACH

We introduce first the fluorescence-enhancement factor, f_E , the magnitude of which we use to assess the performance of our cavity designs. In steady-state conditions, it is defined as the fluorescent count rate per emitter within the nanostructure, normalized to a reference configuration (usually in free space) [25]. In the weak-excitation regime

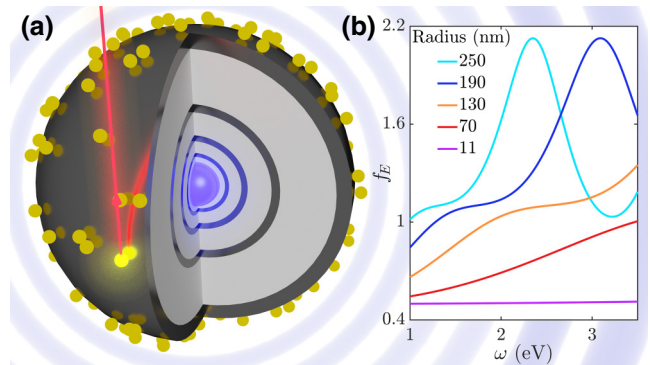


FIG. 1. (a) The hyperbolic nanocavities studied: a silica core is surrounded by spherical silver (black) and silica (gray) layers. The positron emission (red) of radioisotopes (yellow) attached at the outer surface of the structure triggers the fluorescence (violet) of an emitter placed at its center. (b) Fluorescence-enhancement spectra of purely SiO_2 nanospheres of various sizes normalized to free space. These are taken as a reference for the assessment of the performance of the metallocdielectric hyperbolic cavities.

(below fluorescence saturation), it can be expressed as

$$f_E = \left(\frac{|\mathbf{E}|}{|\mathbf{E}_0|} \right)^2 \times \frac{\phi}{\phi_0}. \quad (1)$$

The first term in Eq. (1) accounts for the gain in the excitation (or absorption) efficiency. It is given by the ratio between the electric field intensity at the position of the fluorescent molecule in the presence and the absence of the nanocavity (we assume a random orientation of the emitter). In our case, the EM source triggering CL and fluorescence is β particles from radioactive decay, and we take lossless dielectric nanospheres (of the same size as the nanocavities) as a reference. Silica nanoparticles are widely used in medical imaging research [5]. The second term reflects the loss in the fluorescence quantum yield. We consider emitters with an intrinsic radiative efficiency of 100%, which implies that $\phi/\phi_0 = \phi < 1$. By ignoring the Stokes shift, the fluorescence and absorption bands overlap, which allows us to evaluate the excitation efficiency and quantum-yield loss at the same frequency. Despite its simplicity, Eq. (1) has made possible an accurate description of the fluorescent control [26] enabled by plasmonic nanoantenna geometries [27,28].

Figure 1(a) shows the cavity geometry studied, for which we obtain the solutions of Maxwell's equations required to evaluate Eq. (1). The structure comprises a silica core ($n = 1.5$) or radius $R_{in} = 11$ nm surrounded by a number of alternating silver (with permittivity taken from Ref. [29]) and silica layers. A fluorescent molecule, whose radiative emission is modeled through an EM point-dipole source, is placed at the center of the cavity. Radionuclides are attached at the outer surface of the structure, of radius R_{tot} . Their β decay and associated CL are described by

means of a single-positron line current tangential to the cavity surface and located 3 nm from it. We set the positron kinetic energy to 50 keV, well below the CL threshold in water (261 keV), in our calculations.

Using the spherical symmetry of the system, we can develop a quasianalytic approach based on an EM-field expansion in terms of vector spherical harmonics [30]. A detailed description of the calculations can be found in Supplemental Material [31], and here we outline only their main aspects. The first step of the method consists in expressing the electric field within the spherical layer (labeled as n) as

$$\mathbf{E}_{\alpha,n}(\mathbf{r}) = \sum_{l,m} [A_{\alpha,l,m}(n) \mathbf{J}_{\alpha,l,m}(k_n, \mathbf{r}) + B_{\alpha,l,m}(n) \mathbf{H}_{\alpha,l,m}(k_n, \mathbf{r})], \quad (2)$$

where α stands for the TE or TM mode, and l and m stand for the usual angular-momentum indices. $\mathbf{J}_{\alpha,l,m}$ and $\mathbf{H}_{\alpha,l,m}$ are the vector spherical harmonics, whose radial dependence is given by spherical Bessel and Hankel functions of the first kind. This wave-function choice sets the direction of power-flow propagation in the positive radial direction.

The second step of the approach introduces a set of boundary matrices expressing the EM continuity conditions and relating the electric field amplitudes in two adjacent layers $[A_{\alpha,l,m}(n+1) B_{\alpha,l,m}(n+1)]^\top = T_{\alpha,l}^+(n) [A_{\alpha,l,m}(n) B_{\alpha,l,m}(n)]^\top$, which allows us to link fields at the nanocavity center ($n=1$) and outside ($n=N+2$) through the ordered product

$$\mathcal{M}_{\alpha,l} = T_{\alpha,l}^+(N+1) T_{\alpha,l}^+(N) \dots T_{\alpha,l}^+(2) T_{\alpha,l}^+(1). \quad (3)$$

The shell of the hyperbolic nanocavities is formed by N metallocodielectric layers. Once we have built this ordered-product transfer matrix, we can express the field enhancement, the radiative Purcell factor (\mathcal{P}_R), and the total Purcell factor (\mathcal{P}_T) [26] as

$$\frac{|\mathbf{E}|}{|\mathbf{E}_0|} = \frac{|\langle \mathcal{M}_{E,1}^0 \rangle_{11}|}{|\langle \mathcal{M}_{E,1} \rangle_{11}|}, \quad (4)$$

$$\mathcal{P}_R = \left| \frac{\det \mathcal{M}_{E,1}}{\det \mathcal{M}_{E,1}^0} \right|^2 \left| \frac{\langle \mathcal{M}_{E,1}^0 \rangle_{11}}{\langle \mathcal{M}_{E,1} \rangle_{11}} \right|^2, \quad (5)$$

$$\mathcal{P}_T = \text{Re} \left(1 - \frac{\langle \mathcal{M}_{E,1} \rangle_{12}}{\langle \mathcal{M}_{E,1} \rangle_{11}} \right) / \text{Re} \left(1 - \frac{\langle \mathcal{M}_{E,1}^0 \rangle_{12}}{\langle \mathcal{M}_{E,1}^0 \rangle_{11}} \right), \quad (6)$$

where $\langle \mathcal{M} \rangle_{ij}$ denotes the element in the i th row and j th column of \mathcal{M} . Only TE modes with $l=1$ contribute to the EM fields in Eq. (2); see Ref. [31]. Once we have these

expressions, we can easily evaluate Eq. (1) as the product of Eq. (4) squared and $\phi = \mathcal{P}_R/\mathcal{P}_T$, obtained from Eqs. (5) and (6).

The zero subscript and superscripts in Eqs. (4)–(6) denote reference quantities. As anticipated, we normalize our results to fluorescence-enhancement factors in SiO_2 spheres. This way, we avoid a rather unfeasible system, a free-standing fluorescent agent and a distant β particle traveling in free space. Figure 1(b) shows the fluorescence-enhancement spectra for silica spheres of different R_{tot} (between 11 and 250 nm) now normalized to free space. We observe that $0.4 < f_E < 1$ for subwavelength spheres, whereas moderate ($f_E \simeq 2$) fluorescence maxima emerge in larger structures due to the excitation of Mie resonances [32]. The small deviations from the freestanding configuration allow us to safely take these lossless dielectric particles as the reference system in our assessment of our hyperbolic nanocavity designs.

III. PERIODIC NANOCAVITIES

We apply the theoretical framework introduced in the previous section to investigate periodic cavities, studied recently in the context of low-threshold lasing [33] and second-harmonic generation [34]. If the shell period, the distance between consecutive layers of the same material ($2d = R_{n+2} - R_n$), is much smaller than the operating wavelength, a metamaterial description of the structure [20] is possible. Borrowing the expressions for their bulk, planar counterpart [21], we can write $\epsilon_r = \epsilon_{\text{Ag}} \epsilon_{\text{SiO}_2} / [(1-\eta)\epsilon_{\text{Ag}} + \eta\epsilon_{\text{SiO}_2}]$ and $\epsilon_t = \eta\epsilon_{\text{Ag}} + (1-\eta)\epsilon_{\text{SiO}_2}$ for the radial and tangential permittivity components, respectively, of the metallocodielectric shell around the SiO_2 core (η denotes the silver filling fraction). We focus our attention on geometries in which the Ag and SiO_2 layers have exactly the same thickness, so $\eta = 0.5$ and $d = R_{n+1} - R_n$. At frequencies below 3.8 eV, the silver plasma frequency [29], $\text{Re}(\epsilon_r \epsilon_t) = \text{Re}(\epsilon_{\text{Ag}}) \epsilon_{\text{SiO}_2} < 0$, which reflects the hyperbolic character of the cavities.

Figure 2 provides a comprehensive perspective on the spectral characteristics of hyperbolic cavities with $\eta = 0.5$ and different dimensions. The size of the structures is given by $R_{\text{tot}} = R_{\text{in}} + Nd$, where $R_{\text{in}} = 11$ nm is the silica-core radius and N is the number of layers forming the shell. The columns indicate N ranging from 1 (left) to 7 (right), whereas each row displays a different magnitude (from top to bottom): field enhancement, $|\mathbf{E}|/|\mathbf{E}_0|$, radiative Purcell factor, \mathcal{P}_R , quantum yield, ϕ , and fluorescence enhancement, f_E . The EM response of core-shell nanoparticles [35] ($N=1$) is the weakest. Only below 30 nm (see the insets, left column) does the silver thickness become comparable to the skin depth, and the effect of localized plasmonic resonances becomes apparent in all panels slightly above 3 eV. These are excited by the evanescent tail of the

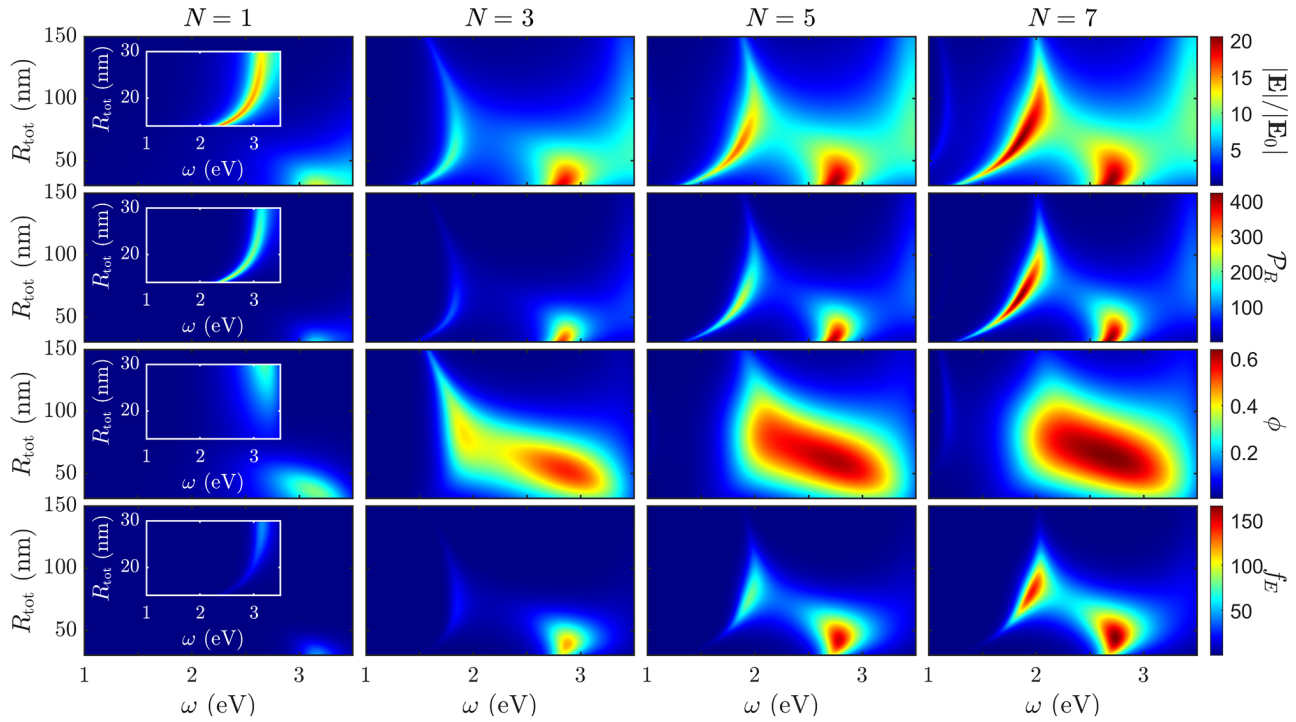


FIG. 2. Field-enhancement, radiative-Purcell-factor, quantum-yield and fluorescence-enhancement maps versus frequency, ω , and cavity size, R_{tot} , are shown from top to bottom for core-shell cavities ($N = 1$) and hyperbolic cavities with $N = 3, 5$, and 7 metallocodielectric layered shells (from left to right).

positron fields, rather than freely propagating Cerenkov radiation. Because of plasmon hybridization effects, the peaks associated with these confined modes undergo a red shift with decreasing thickness [36]. Even in this regime, $f_E < 50$ due to the strong impact of optical absorption on ϵ_{Ag} , which severely reduces the effective quantum yields in the visible range.

The panels in the three rightmost columns in Fig. 2 demonstrate that the performance of hyperbolic cavities is qualitatively different from that of core-shell nanoparticles. They also reveal that their spectral properties are remarkably similar for all N . Two field-enhancement and radiative-Purcell-factor maxima are apparent in the upper rows, which are sharper and stronger for P_R and larger N . The high-frequency one ($\omega \approx 2.7$ eV) fades away for $R_{\text{tot}} > 50$ nm, whereas the low-frequency one ($\omega \approx 1.8$ eV) is clearly visible up to much larger structures, and shifts in a nonmonotonic fashion as the size of the cavity increases. We anticipate that these two spectral features originate from optical resonances of different nature. Between them, the quantum-yield maps develop a broad maximum ($\phi \approx 0.6$), a direct consequence of the lower impact of metal absorption, and therefore lower P_T in this region. The f_E contour plots show that, as expected from the upper maps, the fluorescence spectrum of periodic shell cavities is governed by the high-frequency resonance for $R_{\text{tot}} \leq 50$ nm and by

low-frequency resonance for $50 \text{ nm} < R_{\text{tot}} \leq 120 \text{ nm}$. For larger cavity sizes, much lower fluorescence-enhancement factors are obtained.

To gain further insight into the nature of the optical resonances sustained by the periodic cavities in Fig. 2, we display in Figs. 3(a) and 3(b) electric-field-amplitude color maps (on a log scale) for the maxima in the fluorescence-enhancement spectrum for $N = 7$ and $R_{\text{tot}} = 60$ nm (7-nm-thick layers) at $\omega = 1.8$ eV [Fig. 3(a)] and $\omega = 2.7$ eV [Fig. 3(b)]. To facilitate the comparison, we set $\log_2 |\mathbf{E}| = 3.5$ at the core of the cavity, in which both resonant fields are rather uniform. Through the spatial distribution of $|\mathbf{E}|$, we can infer the character of the two resonances. At $\omega = 1.8$ eV, the electric field is strongly amplified within the first (and second) innermost silica layers. In contrast, the amplitude maxima are located at the inner and outer boundaries of the innermost metallic layer at $\omega = 2.7$ eV. This enables us to identify the former as a dielectric whispering-gallery mode [33], and the latter as a localized-surface-plasmon mode [36]. Importantly, this interpretation of both resonances is also in agreement with the evolution of the field enhancement and radiative-Purcell-factor peaks with increasing R_{tot} in Fig. 2.

The contour plots in Figs. 3(a) and 3(b) are obtained by means of numerical simulations performed with the finite-element solver of Maxwell's equations implemented in COMSOL MULTIPHYSICS. Figure 3(c) demonstrates

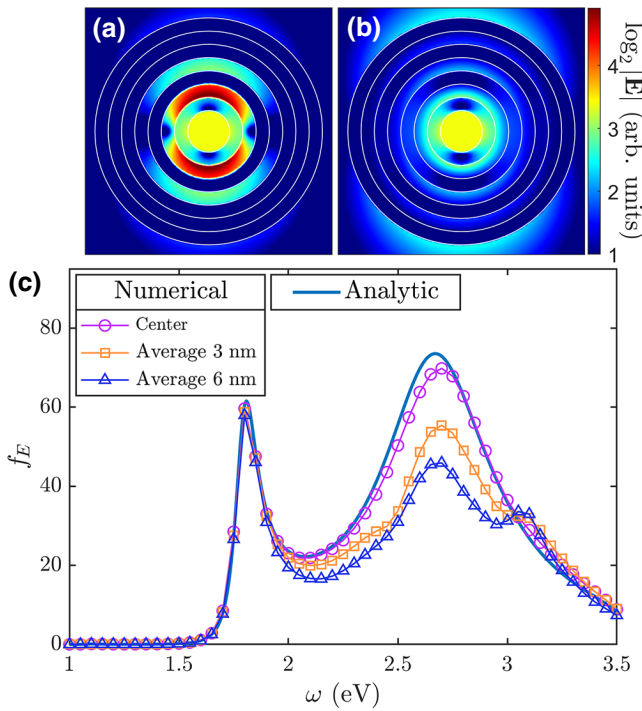


FIG. 3. Electric-field-amplitude maps for the two f_E peaks, $\omega = 1.8$ eV (a) and $\omega = 2.7$ eV (b), in the spectrum of a seven-layer hyperbolic cavity with $R_{\text{tot}} = 60$ nm. The layer boundaries are shown as white lines. (c) The solid blue line and the violet circles plot the fluorescence-enhancement spectra for an emitter placed at the center of the silica core. The former represents transfer-matrix results and the latter represent fully numerical simulations. Orange squares and dark-blue triangles plot numerical fluorescence-enhancement spectra obtained by the spatial and orientational averaging of the fluorescent molecule up to 3 and 6 nm from the cavity center.

the excellent agreement between the fluorescence-enhancement spectra (for the same nanocavity geometry) calculated with this computational tool (violet circles) and with our quasianalytic transfer-matrix approach (solid blue line). Up to here, we assume that the fluorescent dye is placed exactly at the center of the nanostucture. We assess the robustness of our findings against variations in the emitter position through the spectra shown by orange squares and dark-blue triangles in Fig. 3(c). These two sets of data are obtained through the spatial and orientational averaging of f_E numerical calculations up to 3 nm (squares) and 6 nm (triangles) from the core center. As expected, the whispering-gallery-like mode at 1.8 eV [Fig. 3(a)] is insensitive to this averaging. In contrast, the evanescent character of the plasmon modes at higher frequencies translates into a strong alteration of the fluorescence-enhancement spectrum. Thus, by displacement of the emitter away from the cavity center, the broad f_E maximum at 2.7 eV [Fig. 3(b)] is fragmented into sharper features. This indicates

that, similarly to other cavity geometries [37], dark localized plasmon resonances with higher angular momenta (more tightly confined to the silica-silver interface at the external boundary of the cavity core) are excited this way.

Two practical aspects regarding the implementation of the cavity geometry in Fig. 3 are analyzed in Supplemental Material [31]. On the one hand, the robustness of the design against metallic losses is assessed. We show that silver structures, which would require an external coating to increase their biocompatibility [38,39], significantly outperform gold ones. On the other hand, the characterization of the devices by means of electron-energy-loss microscopy [40] is explored. We conclude that it would not be a suitable tool for this purpose, as it is extremely sensitive to dark EM modes that do not contribute to the f_E spectrum.

IV. OPTIMIZED NANOCAVITIES

Taking advantage of the quasianalytic character of our transfer-matrix approach, we investigate next the optimization of hyperbolic cavity geometries. Specifically, we seek the highest fluorescence-enhancement factor achievable at a given optimization (or operation) frequency, ω_{opt} , through the appropriate tuning of the various thicknesses in the multilayer shell. Thus, we set an N -dimensional (where N is the number of layers) problem, which we tackle through interfacing a PSO algorithm [41,42] with our transfer-matrix framework. Very briefly, PSO is a stochastic population-based method that improves candidate solutions in an iterative manner. The optimization occurs through the guided sampling of the parameter space by each individual solution candidate by means of simple dynamical equations. The method has attracted much attention lately due to its versatility and relatively easy implementation in areas such as biomedicine, antenna design, and electromagnetism [43]. See Supplemental Material [31] for more technical details on the PSO algorithm we use in our investigation.

Figure 4(a) presents the outcome of the geometry optimization of seven-layered hyperbolic cavities ($R_{\text{in}} = 11$ nm in all designs). It displays f_E spectra as a function of the optimization frequency. We extend the frequency window down to 0.5 eV, where the performance of perfectly periodic shells is very poor; see Fig. 2. The dotted black line plots the condition $\omega = \omega_{\text{opt}}$, along which the fluorescence-enhancement spectrum develops its main peak. This feature governs the cavity performance for all ω_{opt} values, in contrast with periodic geometries, where two different peaks (of different nature) are found. The dashed white lines plot the frequencies of the relevant optical resonances sustained by the PSO-designed cavities. These are obtained through the condition $\langle \mathcal{M}_{E1} \rangle_{11} = 0$, which yields the nonzero TE solutions (well behaved at the cavity center) of the homogeneous

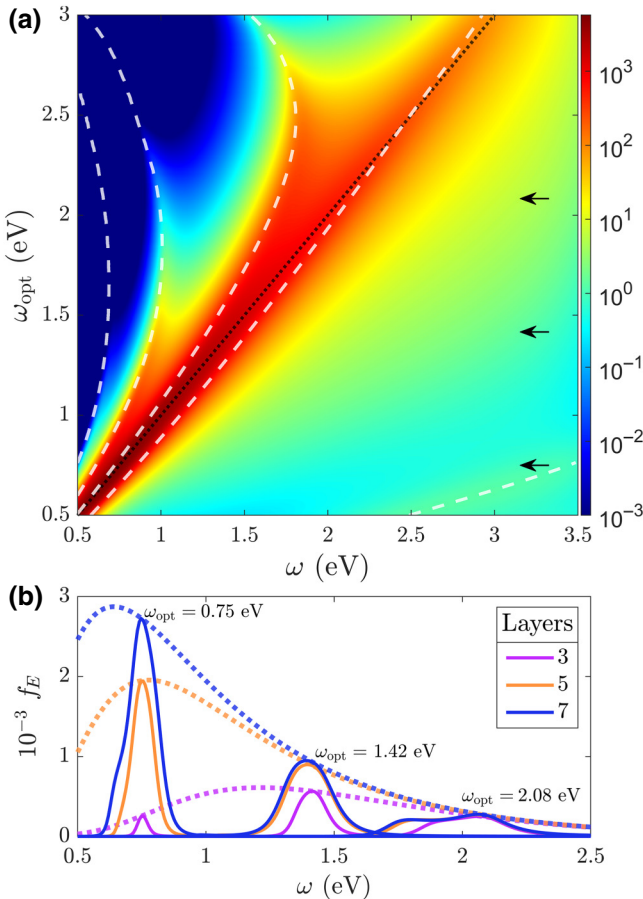


FIG. 4. (a) PSO fluorescence-enhancement spectra as a function of the optimization frequency for a seven-layer nanocavity ($R_{in} = 11$ nm). The dotted black line plots the condition $\omega = \omega_{opt}$, and dashed white lines plot the frequencies of the various optical resonances sustained by the nanostructures. (b) f_E spectra for PSO-designed cavities with seven (blue), five (orange), and three (violet) metalodielectric layers and three different values of ω_{opt} , 0.75, 1.42, and 2.08 eV, indicated by the horizontal black arrows in (a). Dotted lines represent the fluorescence-enhancement factor along the line $\omega = \omega_{opt}$ and for different N .

transfer-matrix equation. This equation is formally equivalent to the scattering resonant condition in the Mie formalism [32]; see Supplemental Material [31] for more details. Figure 4(a) reveals that the f_E maximum in PSO-designed cavities emerges from the spectral overlap and hybridization of various optical resonances. At high ω_{opt} , this mechanism is not very efficient, and we identify the f_E peak as the localized-surface-plasmon resonance in Fig. 3(b). For lower optimization frequencies, and in the region $\omega < \omega_{opt}$, other whispering-gallery-like resonances become apparent. The PSO algorithm results in a redshift of these modes through the cavity geometry and forces them to coalesce into the main f_E peak at $\omega = \omega_{opt}$.

To evaluate the efficiency of the resonance hybridization and spectral overlapping done by the PSO algorithm, Fig. 4(b) shows fluorescence-enhancement spectra at three different values of ω_{opt} : 0.75, 1.42, and 2.08 eV. These are indicated by horizontal black arrows in Fig. 4(a). Blue lines correspond to seven-layered cavities [as in Fig. 4(a)], and violet and orange lines correspond to three- and five-layered cavities, respectively. We observe that spectra for different values of ω_{opt} do not overlap, due to the inherent single-peaked character. However, the maxima become stronger and narrower as the optimization frequency is reduced. This trend is similar for all values of N , but the height contrast is much larger for seven-layered cavities than for three-layered cavities. Notice that two distinct features, resembling Fig. 3(c), are apparent for $N = 5$ and $N = 7$ at $\omega_{opt} = 2.08$ eV. Dotted lines plot the fluorescence-enhancement factor evaluated at $\omega = \omega_{opt}$, demonstrating that the maximum fluorescence enhancement attainable at a given N not only increases but also undergoes a red shift with increasing number of layers. These observations are in accordance with our interpretation of the effect of the PSO algorithm on the cavity design, as the number of resonances that can be merged becomes larger with lower ω_{opt} and higher N .

Once we analyze the spectral properties of the PSO-designed cavities, we explore next their geometric characteristics as well as the spatial distribution of the resonant EM fields that they sustain. Figures 5(a)–5(c) display the electric field amplitude evaluated at $\omega = \omega_{opt}$ for the $N = 7$ cavities obtained for the optimization frequencies in Fig. 4(b): 0.75, 1.42, and 2.08 eV. $|E|$ is on a log scale and normalized to the same value at the core center in Figs. 5(a)–5(c). We observe remarkable differences between the three designs. The relative thickness of the Ag layers increases significantly with larger ω_{opt} , while the overall cavity size is strongly reduced. Figures 5(a)–5(c) are scaled so that horizontal white bars are 100 nm long in all cases. This trend in structural geometry is accompanied by a gradual modification of the optical resonance behind the f_E maxima. The electric field is almost completely confined at the second SiO_2 layer in Fig. 5(a), while it spreads over all the dielectric regions in Fig. 5(b). In contrast, the electric field map in Fig. 5(c) penetrates considerably within the silver layers, and presents an intense evanescent tail spilling out of the cavity. This phenomenology indicates that, as we had anticipated, the hybridized optical resonances supported by these PSO-designed cavities have mainly a whispering-gallery-like character at 0.75 eV, and a localized-surface-plasmon nature at 2.08 eV.

We present next a more-general view on the evolution of the geometric parameters of the cavity with increasing ω_{opt} (for a different number of layers). Figure 5(d) shows that the nanostructures shrink monotonically as ω_{opt} increases. At high frequencies, R_{tot} is the same for all values of N , as localized-plasmon modes are rather

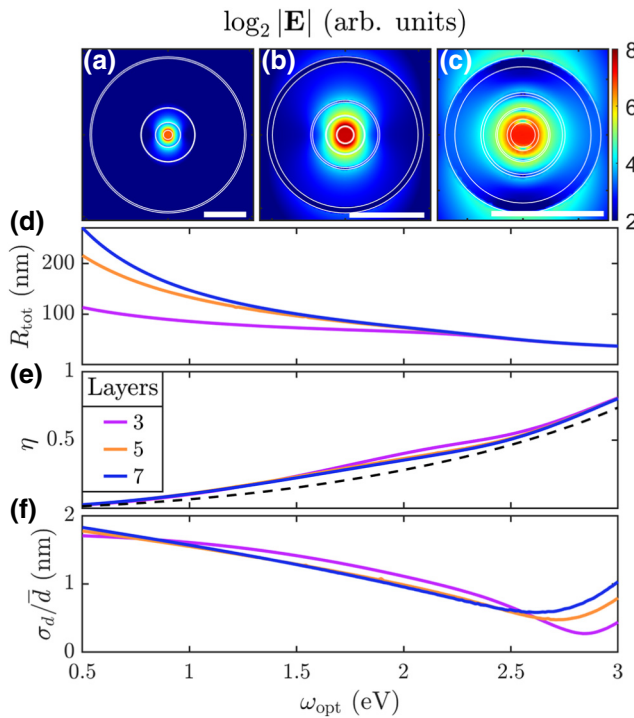


FIG. 5. (a)–(c) Resonant-electric-field amplitude (on a log scale) for $N = 7$ PSO-designed cavities at three different operating frequencies: 0.75 eV (a), 1.42 eV (b), and 2.08 eV (c). The multilayer geometric boundaries are shown as white lines. The white scale bar is 100 nm long in (a)–(c). (d) Outer radius, R_{tot} , versus optimization frequency for three-, five-, and seven-layered cavities. (e) Silver filling fraction as a function of ω_{opt} and N . The dashed black line plots $\eta(\omega_{\text{opt}}) = 2\eta_{\epsilon_l=0}(\omega_{\text{opt}})$; see the main text. (f) Normalized standard deviation of the multilayer-thickness distribution for PSO-designed cavities with different values of N .

insensitive to the silica-layer distribution. However, strong differences become evident at low frequencies. While R_{tot} is scaled by a factor of approximately 5 with respect to the high-frequency range in seven-layered geometries, it experiences only a twofold enlargement for $N = 3$. This observation, together with the low fluorescence-enhancement maxima in Fig. 4(b), proves there is little margin for geometry optimization in three-layered cavities operating in the infrared region.

Figure 5(e) plots the silver filling fraction versus ω_{opt} , which is extremely similar for all values of N . It grows from negligible η at low frequencies (Ag layers are extremely thin in these designs) to $\eta \simeq 0.8$ at 3 eV, which is also in accordance with our interpretation of the character of the cavity resonances (from whispering-gallery-like to localized-plasmon-like modes). Although it is evident that an homogeneous metamaterial treatment of PSO-designed cavities cannot be accurate, we can use it to gain further insights into their performance. We find that the curves in Fig. 5(e) lie very close to the condition $\eta(\omega_{\text{opt}}) = 2\eta_{\epsilon_l=0}(\omega_{\text{opt}})$ (rendered as a dotted black line),

where $\eta_{\epsilon_l=0} = \epsilon_{\text{SiO}_2}/[\epsilon_{\text{SiO}_2} - \text{Re}[\epsilon_{\text{Ag}}(\omega_{\text{opt}})]]$ is the filling fraction that cancels the real part of the tangential metamaterial permittivity. Inserting $\eta(\omega_{\text{opt}})$ into the expressions for the radial and tangential permittivities, we find that $\epsilon_r(\omega_{\text{opt}})\epsilon_t(\omega_{\text{opt}}) \simeq -\epsilon_{\text{Ag}}(\omega_{\text{opt}})\epsilon_{\text{SiO}_2}^2/[\epsilon_{\text{Ag}}(\omega_{\text{opt}}) + 2\epsilon_{\text{SiO}_2}]$, whose real part is negative for $\omega_{\text{opt}} < 3.8$ eV. Therefore, we can argue that PSO designs perform as hyperbolic cavities within the visible and near-infrared regions despite their structural inhomogeneity. Figure 5(f) provides a measure of this inhomogeneity; it shows the normalized standard deviation in the layer-thickness distribution (\bar{d} denotes the mean layer thickness) as a function of ω_{opt} and N . Only at $\omega_{\text{opt}} \simeq 2.5$ eV do we find $\sigma_d \lesssim \bar{d}$, which sets the frequency range in which the PSO-designed cavities are most homogeneous, most similar to a perfectly periodic geometry ($\sigma_d = 0$). A more-detailed analysis of the multilayer-thickness distribution as a function of the operating frequency can be found in Supplemental Material [31].

V. CONCLUSIONS

We investigate the performance of hyperbolic nanocavities, nanostructures formed by a silica core and an arrangement of alternating silver and silica layers, for fluorescence-imaging applications. We focus on a particular configuration: the emission by a fluorescent agent located at the cavity center triggered by the positrons generated in the β decay of radionuclides attached at the cavity outer surface. We report a 100-fold enhancement in perfectly periodic geometries, and up to a 10 000-fold fluorescence amplification in particle-swarm-optimized cavities. The hybrid (whispering-gallery and localized-plasmon) nature of the optical resonances sustained by these structures and their tuning through geometry are also analyzed in detail. We believe that our theoretical findings present an avenue for the development of nuclear-optical imaging techniques using not only the Cerenkov luminescence naturally occurring in the decay of radiotracers but also the visible and infrared light generated by fluorescent agents in their vicinity.

ACKNOWLEDGMENTS

This work was funded by the Spanish Ministry of Science and Innovation under Contract No. TI2018-099737-B-I00 and through the María de Maeztu program for units of excellence in R&D (CEX2018-000805-M). It was also supported by the European Union QuantERA program through project PCI2018-093145, and by an NIH Cancer Center Support grant (P30 CA008748) and an NIH grant to J.G. (1R01CA183953-01A1). J.A.-A. acknowledges funding from the Spanish MECD (FPU18/05912 scholarship). V.M.M. acknowledges support of the National Science Foundation through Grant No. DMR-1709996. A.I.F.-D.

was supported by a 2019 Leonardo Grant for researchers and cultural creators from the BBVA Foundation.

-
- [1] P. A. Cerenkov, Visible radiation produced by electrons moving in a medium with velocities exceeding that of light, *Phys. Rev.* **52**, 378 (1937).
- [2] G. S. Mitchell, R. K. Gill, D. L. Boucher, C. Li, and S. R. Cherry, In vivo Cerenkov luminescence imaging: A new tool for molecular imaging, *Phil. Trans. R. Soc. A* **369**, 4605 (2011).
- [3] J. S. Cho, R. Taschereau, S. Olma, K. Liu, Y.-C. Chen, C. K.-F. Shen, R. M. van Dam, and A. F. Chatzioannou, Cerenkov radiation imaging as a method for quantitative measurements of beta particles in a microfluidic chip, *Phys. Med. Biol.* **54**, 6757 (2009).
- [4] R. Robertson, M. S. Germanos, C. Li, G. S. Mitchell, S. R. Cherry, and M. D. Silva, Optical imaging of Cerenkov light generation from positron-emitting radiotracers, *Phys. Med. Biol.* **54**, N355 (2009).
- [5] E. C. Pratt, T. M. Shaffer, Q. Zhang, C. M. Drain, and J. Grimm, Nanoparticles as multimodal photon transducers of ionizing radiation, *Nat. Nanotechnol.* **13**, 418 (2018).
- [6] D. L. J. Thorek, R. Robertson, W. A. Bacchus, J. Hahn, J. Rothberg, B. J. Beattie, and J. Grimm, Cerenkov imaging – a new modality for molecular imaging, *Am. J. Nucl. Med. Mol. Imaging* **2**, 163 (2012).
- [7] T. M. Shaffer, E. C. Pratt, and J. Grimm, Utilizing the power of Cerenkov light with nanotechnology, *Nat. Nanotechnol.* **12**, 106 (2017).
- [8] I. Frank and I. Tamm, Coherent visible radiation of fast electrons passing through matter, *Comptes Rendus (Dokl.) Acad. Sci. URSS* **14**, 109 (1937).
- [9] P. T. K. Chin, M. M. Welling, S. C. J. Meskers, R. A. Valdes Olmos, H. Tanke, and F. W. B. van Leeuwen, Optical imaging as an expansion of nuclear medicine: Cerenkov-based luminescence vs fluorescence-based luminescence, *Eur. J. Nucl. Med. Mol. Imaging* **40**, 1283 (2013).
- [10] F. Liu, L. Xiao, Y. Ye, M. Wang, K. Cui, X. Feng, W. Zhang, and Y. Huang, Integrated Cerenkov radiation emitter eliminating the electron velocity threshold, *Nat. Photonics* **11**, 289 (2017).
- [11] P. Genevet, D. Wintz, A. Ambrosio, A. She, R. Blanchard, and F. Capasso, Controlled steering of Cherenkov surface plasmon wakes with a one-dimensional metamaterial, *Nat. Nanotech.* **10**, 804 (2015).
- [12] J.-K. So, J.-H. Won, M. A. Sattorov, S.-H. Bak, K.-H. Jang, G.-S. Park, D. S. Kim, and F. J. García-Vidal, Cerenkov radiation in metallic metamaterials, *Appl. Phys. Lett.* **97**, 151107 (2010).
- [13] V. Ginis, J. Danckaert, I. Veretennicoff, and P. Tassan, Controlling Cherenkov Radiation with Transformation-Optical Metamaterials, *Phys. Rev. Lett.* **113**, 167402 (2014).
- [14] X. Lu, M. A. Shapiro, I. Mastovsky, R. J. Temkin, J. G. Power, J. Shao, E. E. Wisniewski, and C. Jing, Generation of High-Power, Reversed-Cerenkov Wakefield Radiation in a Metamaterial Structure, *Phys. Rev. Lett.* **112**, 014801 (2019).
- [15] J. Tao, Q. J. Wang, J. J. Zhang, and Y. Luo, Reverse surface-polariton Cherenkov radiation, *Sci. Rep.* **6**, 30704 (2016).
- [16] I. Kaminer, Y. T. Katan, H. Buljan, Y. Shen, O. Illic, J. J. López, L. J. Wong, J. D. Joannopoulos, and M. Soljacic, Efficient plasmonic emission by the quantum Cerenkov effect from hot carriers in graphene, *Nat. Commun.* **7**, 11880 (2016).
- [17] I. Kaminer, S. E. Kooi, R. Shiloh, B. Zhen, Y. Shen, J. J. López, R. Remez, S. A. Skirlo, Y. Yang, J. D. Joannopoulos, A. Arie, and M. Soljacic, Spectrally and Spatially Resolved Smith-Purcell Radiation in Plasmonic Crystals with Short-Range Disorder, *Phys. Rev. X* **7**, 011003 (2017).
- [18] D. L. J. Thorek, A. Ogirala, B. J. Beattie, and J. Grimm, Quantitative imaging of disease signatures through radioactive decay signal conversion, *Nat. Med.* **19**, 1345 (2013).
- [19] R. S. Dothager, R. J. Goiffon, E. Jackson, S. Harpstite, and D. Piwnica-Worms, Cerenkov radiation energy transfer (CRET) imaging: A novel method for optical imaging of PET isotopes in biological systems, *PLoS ONE* **5**, e13300 (2010).
- [20] C. Wu, A. Salandrinno, X. Ni, and X. Zhang, Electrodynamical Light Trapping Using Whispering-Gallery Resonances in Hyperbolic Cavities, *Phys. Rev. X* **4**, 021015 (2014).
- [21] L. Ferrari, C. Wu, D. Lepage, X. Zhang, and Z. Liu, Hyperbolic metamaterials and their applications, *Prog. Quantum Electron.* **40**, 1 (2015).
- [22] Z. S. Wu, L. X. Guo, K. F. Ren, G. Gouesbet, and G. Gréhan, Improved algorithm for electromagnetic scattering of plane waves and shaped beams by multilayered spheres, *Appl. Opt.* **36**, 5188 (1997).
- [23] A. Moroz, A recursive transfer-matrix solution for a dipole radiating inside and outside a stratified sphere, *Ann. Phys.* **315**, 352 (2005).
- [24] J. Kennedy and R. Eberhart, in *IEEE International Conference on Neural Networks – Conference Proceedings* (Piscataway, NJ, IEEE, 1995).
- [25] P. Bharadwaj and L. Novotny, Spectral dependence of single molecule fluorescence enhancement, *Opt. Express* **15**, 14266 (2007).
- [26] V. Giannini, A. I. Fernández-Domínguez, S. C. Heck, and S. A. Maier, Plasmonic nanoantennas: Fundamentals and their use in controlling the radiative properties of nanoemitters, *Chem. Rev.* **111**, 3888 (2011).
- [27] A. Kinkhabwala, Z. Yu, S. Fan, Y. Avlasevich, K. Müllen, and W. E. Moerner, Large single-molecule fluorescence enhancements produced by a bowtie nanoantenna, *Nat. Photonics* **3**, 654 (2009).
- [28] G. P. Acuña, F. M. Möller, P. Holzmeister, S. Beater, B. Lalkens, and P. Tinnefeld, Fluorescence enhancement at docking sites of DNA-directed self-assembled nanoantennas, *Science* **338**, 506 (2012).
- [29] A. D. Rakić, A. B. Djurišić, J. M. Elazar, and M. L. Majewski, Optical properties of metallic films for vertical-cavity optoelectronic devices, *Appl. Opt.* **37**, 5271 (1998).
- [30] J. D. Jackson, *Classical Electrodynamics* (Wiley, New York, 1999).
- [31] See Supplemental Material at <http://link.aps.org/supplemental/10.1103/PhysRevApplied.14.024084> for a detailed description of our quasianalytic transfer-matrix approach,

- further insights into the geometric and spectral properties of optimized nanocavities, and the particle-swarm optimization algorithm used.
- [32] G. Mie, Beiträge zur optik trüber medien, speziell kolloidaler Metallösungen, *Ann. Phys.* **25**, 377 (1908).
 - [33] M. Wan, P. Gu, W. Liu, Z. Chen, and Z. Wang, Low threshold spaser based on deep-subwavelength spherical hyperbolic metamaterial cavities, *App. Phys. Lett.* **110**, 031103 (2017).
 - [34] W. Wu, L. Fan, W. Zang, X. Yang, P. Zhan, Z. Chen, and Z. Wang, Second harmonic generation enhancement from a nonlinear nanocrystal integrated hyperbolic metamaterial cavity, *Opt. Express* **25**, 21342 (2017).
 - [35] C. L. Nehl, N. K. Grady, G. P. Goodrich, F. Tam, N. J. Halas, and J. H. Hafner, Scattering spectra of single gold nanoshells, *Nano Lett.* **4**, 2355 (2004).
 - [36] E. Prodan, C. Radloff, N. J. Halas, and P. A. Nordlander, Hybridization model for the plasmon response of complex nanostructures, *Science* **302**, 419 (2003).
 - [37] R.-Q. Li, D. Hernández-Pérez, F. J. García-Vidal, and A. I. Fernández-Domínguez, Transformation Optics Approach to Plasmon-Exciton Strong Coupling in Nanocavities, *Phys. Rev. Lett.* **117**, 107401 (2016).
 - [38] R. Mahmoudi, S. Aghaei, Z. Salehpour, A. Mousavizadeh, S. S. Khoramrooz, M. T. Sisakht, G. Christiansen, M. Baneshi, B. Karimi, and H. Bardania, Antibacterial and antioxidant properties of phyto-synthesized silver nanoparticles using Lavandula stoechas extract, *Appl. Organometal. Chem.* **34**, e5394 (2019).
 - [39] T. J. Miesen, A. M. Engstrom, D. C. Frost, R. Ajjarapu, R. Ajjarapu, C. N. Liraa, and M. R. Mackiewicz, A hybrid lipid membrane coating ‘shape-locks’ silver nanoparticles to prevent surface oxidation and silver ion dissolution, *RSC Adv.* **10**, 15677 (2020).
 - [40] F. J. García de Abajo, Optical excitations in electron microscopy, *Rev. Mod. Phys.* **82**, 209 (2010).
 - [41] Y. Shi and R. Eberhart, in *IEEE International Conference on Evolutionary Computation Proceedings* (Anchorage, AK, IEEE, 1998).
 - [42] E. Mezura-Montes and C. A. Coello Coello, Constraint-handling in nature-inspired numerical optimization: Past, present and future, *Swarm Evol. Comput.* **1**, 173 (2011).
 - [43] R. Poli, Analysis of the publications on the applications of particle swarm optimisation, *Artif. Evol. Appl.* **28**, 1 (2008).